

# Strain-tunable magnetic correlations in spin liquid candidate $\text{Nb}_3\text{Cl}_8$

Tharindu Fernando\*

Department of Physics, University of Washington, Seattle, WA 98195 USA

Ting Cao

Department of Materials Science and Engineering,  
University of Washington, Seattle, WA 98195 USA

(Dated: January 22, 2026)

Recent research suggests the possibility of the two-dimensional breathing-Kagome magnet  $\text{Nb}_3\text{Cl}_8$  hosting a quantum spin liquid state, warranting further study into its magnetic properties. Using *ab initio* calculations, we show that monolayer  $\text{Nb}_3\text{Cl}_8$  has short-range antiferromagnetic correlations among  $\text{Nb}_3$  trimers with  $S = 1/2$ , and becomes magnetically frustrated due to the underlying effective triangular lattice geometry, and is evidenced by a frustration index of  $f > 1$ . The high-temperature susceptibility shows a negative Weiss temperature from Monte Carlo calculations. Considering spin-orbit coupling, we investigate the magnetic anisotropy, including anisotropic exchange, single-ion anisotropy and the Dzyaloshinskii–Moriya interaction using the four-state energy mapping formalism. Although the elements have relatively small atomic numbers, the Dzyaloshinskii–Moriya interaction is comparable in magnitude to the anisotropic exchange. Additionally, we show that biaxial strain tunes the short-range correlations between antiferromagnetic, paramagnetic and ferromagnetic. These findings strengthen our understanding of  $\text{Nb}_3\text{Cl}_8$  and advance its applications in current condensed matter physics and materials science research, including nanoscale mechanical and spintronics applications.

## I. INTRODUCTION

The study of two-dimensional (2D) magnetic phenomena in quantum materials has attracted significant interest due to its potential to reveal novel quantum states and exotic magnetic properties [1–3]. A central goal is to control and tune magnetic order, which not only enables the exploration of new physical phenomena but also drives the development of advanced technologies and the improvement of existing devices [4, 5]. Magnetic tunability underpins applications in condensed matter physics and materials science, including quantum information science and technology [6, 7], spintronic devices and memory [6, 7], magnetic sensing and imaging [8], and the study of exotic electronic and magnetic phases [1–3]. Frustrated magnets, where competing interactions prevent the system from adopting a simple order, are especially intriguing. They can host exotic states such as spin liquids, which provide insights into high-temperature superconductivity, quantum computation, and other emergent phenomena [9–11].

Niobium halides  $\text{Nb}_3\text{X}_8$  ( $\text{X} = \text{Cl}, \text{Br}, \text{I}$ ), which are van der Waals (vdW) materials, are promising candidates for exploring such quantum phenomena. Their breathing Kagome lattice comprises alternating large and small  $\text{Nb}_3$  triangles. Each small triangle, or  $\text{Nb}_3$  *trimer*, hosts a shared molecular orbital with a  $S = 1/2$  moment [12–24]. Thus, despite the breathing Kagome geometry,  $\text{Nb}_3\text{X}_8$  effectively behaves as a triangular lattice magnet, with each trimer corresponding to one triangle’s vertex (Fig. 1). The triangular lattice geometry naturally

supports magnetic frustration, since spins on an equilateral triangle cannot all align antiferromagnetically. If its magnetic correlations could be tuned between antiferromagnetic and other states,  $\text{Nb}_3\text{X}_8$  would provide an appealing platform for realizing controllable quantum magnetism. Accurate modeling of its magnetic properties is therefore essential for assessing its potential to host exotic quantum states.

In this work, we focus on  $\text{Nb}_3\text{Cl}_8$ , since our *ab initio* screening showed an antiferromagnetic nearest-neighbor exchange ( $J^1$ ), in contrast to the ferromagnetic  $J^1$  found in  $\text{Nb}_3\text{Br}_8$  and  $\text{Nb}_3\text{I}_8$  (see also Ref. [26]). The presence of an antiferromagnetic  $J^1$  on an effective triangular lattice geometry makes  $\text{Nb}_3\text{Cl}_8$  a particularly interesting case for detailed study, as it introduces competing interactions that can lead to enhanced magnetic frustration and unconventional magnetic ground states.

Several additional factors motivate our choice of  $\text{Nb}_3\text{Cl}_8$ .  $\text{Nb}_3\text{Cl}_8$  may host topological flat bands in its electronic dispersion [27–32], which in turn can stabilize strongly correlated insulating phases [12, 16, 33]. It has also been identified as a candidate to realize the Hubbard model [18–20], Mott-insulating behavior [16–21, 34], field-effect transistors [35, 36], topological insulators [37], heterostructure phenomena [38, 39], excitonic effects [40], and charge-ice physics [21]. Magnetically, both bulk and monolayer  $\text{Nb}_3\text{Cl}_8$  are paramagnetic at high temperature [14, 19, 21], with the bulk undergoing a  $\sim 90$  K transition to a nonmagnetic singlet ground state [13–15, 17, 19, 23, 31, 41, 42]. However, the exact magnetic ground state of the monolayer remains unsettled, with reports ranging from ferromagnetic [41, 43] to antiferromagnetic [18, 21–23, 32, 33] and even quantum spin liquid candidates [16–18, 20, 23]. To date, there are very

\* [tharindu@uw.edu](mailto:tharindu@uw.edu)

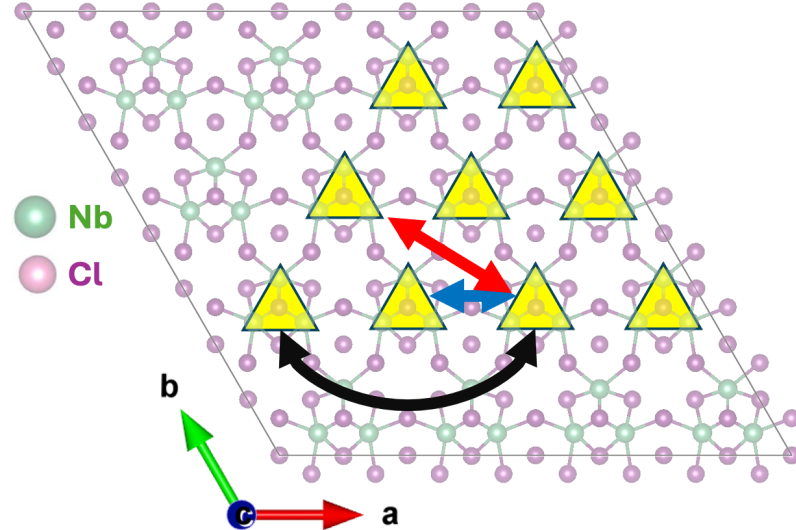


FIG. 1:  $\text{Nb}_3\text{Cl}_8$  crystal structure shown as a  $4 \times 4 \times 1$  supercell, viewed along the  $c$ -axis [25]. Semi-transparent spheres represent Nb (green) and Cl (purple) atoms of the breathing Kagome lattice, with alternating large and small  $\text{Nb}_3$  triangles. Selected  $\text{Nb}_3$  trimers (small triangles, each hosting a single  $S = 1/2$  moment) are highlighted in yellow. Consider each yellow trimer as a single unit that produces the overlying triangular lattice. Arrows indicate NN (blue), 2NN (red), and 3NN (black) trimer-trimer interactions used in our calculations. The triangle with three arrows pointing to it is taken as the first index of each bond.

few studies addressing the impact of spin-orbit coupling (SOC) in the monolayer or exploring how its magnetic correlations can be tuned. Strain is especially important, as it can drive changes in the magnetic ground state as shown in  $\text{CrSBr}$  [44]; yet aside from Ref. [45], which considered strain only in terms of mechanical properties, strain effects in  $\text{Nb}_3\text{Cl}_8$  have not been examined.

In this work, we explore the magnetic properties of monolayer  $\text{Nb}_3\text{Cl}_8$ . Recent studies of the monolayer cover a wide range of topics [16, 18–22, 32, 43, 45], including evidence that its synthesis may be experimentally achievable [22, 32, 43, 45].  $\text{Nb}_3\text{Cl}_8$  belongs to space group 156 (P3m1), which lacks inversion symmetry, permitting nonzero Dzyaloshinskii–Moriya interactions (DMI) in the presence of SOC [46]. SOC further enriches the magnetic landscape by introducing anisotropy and extending the role of extended-neighbor interactions, whose combined influence on magnetic correlations remains unexplored.

A common approach to study magnetic anisotropy is to calculate energy differences among distinct spin configurations. The four-state energy mapping formalism is especially powerful in this regard [47–49]. It reduces ambiguity in near-degenerate cases, accounts comprehensively for interactions (including anisotropic exchange), and, when based on accurate *ab initio* calculations, can yield good agreement with experiment. Yet for  $\text{Nb}_3\text{Cl}_8$ , this formalism has not been applied to the effective triangular lattice formed by  $\text{Nb}_3$  trimers [13, 15, 18, 19, 21, 26, 32, 33, 50].

To address this gap, we employ the four-state mapping method [49] on the triangular trimer lattice to ex-

tract magnetic anisotropy parameters for a generalized Heisenberg-like Hamiltonian [Eq. (1)], including interactions up to third-nearest neighbors. To capture the system’s complexity more accurately, we extend beyond isotropic exchange [13, 15, 18, 19, 21, 26, 32, 33, 50] by incorporating SOC-induced anisotropic exchange (including DMI), and single-ion anisotropy. Using *ab initio* calculations, we determine these parameters within a unified and internally consistent framework, and subsequently calculate the magnetic susceptibility using classical Monte Carlo simulations. Fitting the data to the Curie-Weiss law reveals short-range antiferromagnetic correlations with a negative Weiss temperature, consistent with frustration on the triangular lattice (that is also evidenced by a frustration index of  $f > 1$ ). We also find finite DMI of comparable magnitude to the anisotropic exchange. Finally, we demonstrate that biaxial strain can tune the magnetism between antiferromagnetic, paramagnetic, and ferromagnetic local correlations, providing a route to manipulate the magnetic properties of  $\text{Nb}_3\text{Cl}_8$ .

## II. METHODS

With the anisotropies allowed by SOC, and extended-neighbor interactions, the corresponding generalized Heisenberg-like spin Hamiltonian becomes:

$$H = \sum_{i < j} \mathbf{S}_i \cdot J_{ij}^k \cdot \mathbf{S}_j + \sum_i A_i (S_i^z)^2 \quad (1)$$

where  $k = 1, 2, 3$  corresponds to nearest-neighbor (NN), second-nearest-neighbor (2NN) and third-nearest-neighbor (3NN) pairs respectively. We use the index  $k$  to make explicit the usual  $J^1, J^2, J^3$  notation for NN–3NN couplings.  $\mathbf{S}_i = (S_i^x, S_i^y, S_i^z)$  represents the spin-1/2 at site  $i$ .  $J_{ij}^k$  is the anisotropic exchange interaction between spins at sites  $i$  and  $j$ , and  $A_i$  is the single-ion anisotropy constant at site  $i$ . This form of the single-ion anisotropy contribution to the Hamiltonian is due to the system's easy-plane anisotropy (see next section) [51]. From  $J_{ij}^k$ , we can get the components of the DMI vectors  $D^k = (D_x^k, D_y^k, D_z^k)$  in a Cartesian frame of reference as  $D_x^k = \frac{1}{2}(J_{yz}^k - J_{zy}^k)$ ,  $D_y^k = \frac{1}{2}(J_{zx}^k - J_{xz}^k)$ ,  $D_z^k = \frac{1}{2}(J_{xy}^k - J_{yx}^k)$ .

We note that, to the best of our knowledge, the complete Hamiltonian in Eq. (1), including anisotropic exchange, DMI, and single-ion anisotropy up to third-nearest neighbors, has not been systematically explored in previous studies of spin-1/2 triangular-lattice systems. Earlier works have typically considered simplified models, such as isotropic or XXZ-type exchanges, sometimes including DMI or up to only second-nearest-neighbor interactions, within limited parameter regimes [52–57]. By using the full Hamiltonian, we can capture the combined influence of SOC-induced anisotropies and extended-neighbor couplings on the competition between ferromagnetic and antiferromagnetic correlations, the emergence of noncollinear spin textures, and possible chiral ground states, which cannot always be accessed within the simplified forms.

We used an *ab initio* density functional theory (DFT) approach to perform first-principles DFT+U+SOC calculations. We leave details of our DFT calculations to Supplementary Material A. We used the four-state energy mapping technique to calculate magnetic anisotropy parameters [47–49]. In our calculations, we used the trimer pairs indicated by arrows in Fig. 1 [58].

We used Monte Carlo calculations to obtain magnetic susceptibility as a function of temperature. Then the Curie-Weiss law identifies the role of dominant exchange interactions and suggest possible spin-spin correlations. The magnetic susceptibility  $\chi_d$  (in  $d = x, y, z$  directions) of antiferromagnetic (AFM) and ferromagnetic (FM) materials above their respective critical temperatures (Néel temperature  $T_N$  for antiferromagnets, and Curie temperature  $T_C$  for ferromagnets) is:

$$\frac{1}{\chi_d} = \frac{T - \theta_d}{C}. \quad (2)$$

Above, we have the temperature  $T$ , Curie constant  $C$  and Weiss temperature  $\theta_d$ .  $\theta_d$  is typically negative in AFM states, 0 in paramagnetic (PM) states, and positive in FM states [59]. Although anisotropy, as in the case of this work, may affect long-range magnetic order, the sign and magnitude of  $\theta_d$  still reflect the presence of short-range correlations. We refer the reader to Supplementary Material B for details on our Monte Carlo calculations.

### III. FRUSTRATION AND DZYALOSHINSKII–MORIYA INTERACTION

For the triangle vertex pairs illustrated in Fig. 1, we calculated the following (in units of meV):

$$J^1 = \begin{bmatrix} 1.49 & -0.15 & 0.89 \\ 0.15 & 1.59 & -0.01 \\ -0.89 & -0.01 & 1.47 \end{bmatrix}, J^2 = \begin{bmatrix} 0.96 & 0.00 & 0.04 \\ 0.00 & 0.97 & -0.02 \\ -0.04 & 0.02 & 0.95 \end{bmatrix} \\ J^3 = \begin{bmatrix} -0.73 & 0.00 & 0.00 \\ 0.00 & -0.74 & 0.00 \\ 0.00 & 0.00 & -0.73 \end{bmatrix} \quad (3)$$

where the anisotropic exchange  $J^k$  is (using a Cartesian frame of reference, and ignoring the superscript  $k = 1, 2, 3$  for brevity):

$$J = \begin{bmatrix} J_{xx} & J_{xy} & J_{xz} \\ J_{yx} & J_{yy} & J_{yz} \\ J_{zx} & J_{zy} & J_{zz} \end{bmatrix}. \quad (4)$$

The single-ion anisotropy constant was  $A = 0.56$  meV. The DMI vector  $\mathbf{D}^k = (D_x, D_y, D_z)$  was calculated to be  $\mathbf{D}^1 = (0, -0.89, -0.15)$  meV,  $\mathbf{D}^2 = (-0.02, -0.04, 0)$  meV, and  $\mathbf{D}^3 = (0, 0, 0)$  meV (see Fig. S1). Using the convention dictated by Eq. (1),  $J_{mn}^k > 0$  is an AFM interaction (and  $J_{mn}^k < 0$  is FM), for  $m, n$  being  $x, y, z$ .  $A > 0$  implies easy-plane anisotropy.

Notice that most of the nonzero components of  $J^1$  and  $J^2$  are  $> 0$ , suggesting that they are AFM. Indeed, using our classical Monte Carlo calculations at high-T, we found the Weiss temperatures  $(\theta_x, \theta_y, \theta_z) = (-47.0 \pm 0.5, -46.9 \pm 0.5, -48.8 \pm 0.5)$  K.  $\theta_z$  is different from  $\theta_x$  and  $\theta_y$  due to the in-plane anisotropy. The temperature dependent susceptibility used to calculate  $\theta_d$  is given in Fig. 2 and Fig. S4. In all cases, we obtained an effective moment  $\mu_{\text{eff}} \approx 1.77 \mu_B$ , corresponding to a Landé  $g$ -factor of  $\approx 2.04$ , which is in good agreement with the expected value of  $1.73 \mu_B$  for a spin-1/2 system ( $g \approx 2$ ). These  $\theta_d$  compare well with reported values of isotropic  $\theta$  from Curie-Weiss fittings of susceptibility from experimental single crystal and powder, and theoretical data. These  $\theta$  fall within the range of  $-70.1 < \theta < -13.1$  K [13–15, 17, 19, 23, 26, 32, 60], with the exception of the reported ferromagnetic Weiss temperatures of  $+15$  K (from single crystals) [41] and  $+31$  K (from DFT) [43].

Since all our  $\theta_d < 0$ , we have short-range AFM correlations. The system's clear AFM characteristics above the critical temperature suggests that it could be frustrated due to the triangular lattice structure, as an AFM configuration cannot be fully satisfied in such a geometry. To quantify this, we calculate the frustration index  $f$  [61]:

$$f = -\frac{\theta_d}{T_N}. \quad (5)$$

From our susceptibility plots (e.g., Fig. 2), we found  $T_N \sim 20.2 \pm 0.5$  K (same for all  $x, y, z$  directions within the range of error, as expected). Then, we have

$(f_x, f_y, f_z) \sim (2.3, 2.3, 2.4) \pm 0.1$ , which indicates frustration since  $f > 1$ . This frustration may be a stepping stone towards realizing exotic magnetic phenomena, such as quantum spin liquids.

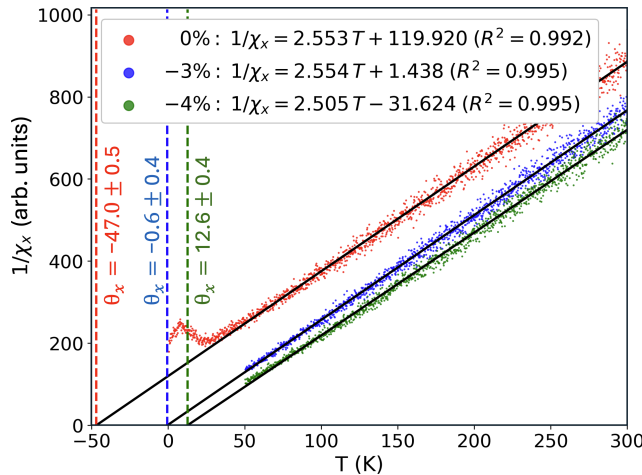


FIG. 2: Inverse magnetic susceptibility  $1/\chi_d$  (arb. units) vs. temperature  $T(K)$  in the  $d = x$ -direction for 0% (unstrained),  $-3\%$ , and  $-4\%$  biaxial strain. Data from Monte Carlo simulations are shown as dots. For clarity in illustration, we show Monte Carlo data for only the  $50 \leq T \leq 300$  K range used in the fitting, with the exception of 0% strain, which exemplifies the kink indicating  $T_N$ . The Weiss temperature  $\theta_d$  and uncertainty for each case is given alongside the vertical dashed lines denoting the intersection of the linear fits with the  $T$  axis.

We note that the calculated DMI vectors are consistent with the symmetry constraints imposed by the crystal (Moriya's rules) and, upon enforcing the full little group at the bond midpoint, reduce to  $D_x^1 = 0$  for the NN bond in direction  $(-1, 0, 0)$ ,  $D_z^2 = 0$  for the 2NN bond in direction  $(-1, 1, 0)$ , and  $D_x^3 = 0$  for the 3NN bond in direction  $(-2, 0, 0)$ , where the bond directions are expressed in the  $(a, b, c)$  lattice basis (see Fig. 1). See Supplementary Material C for a visualization of the DMI. The origin of the DMI symmetry constraints can be understood by considering the site symmetry (little group) at each bond midpoint and applying Moriya's rules for the DMI. For the NN and 3NN bonds oriented along the  $a$ -axis, the relevant vertical mirror plane in P3m1 is perpendicular to the bond and passes through its midpoint. This operation exchanges the two end sites, and the invariance of the antisymmetric exchange term  $\mathbf{D}_{ij} \cdot (\mathbf{S}_i \times \mathbf{S}_j)$  requires the DMI vector to be invariant under this mirror. Because  $\mathbf{D}$  transforms as an axial vector, the component along the bond direction changes sign under reflection and must vanish, hence  $D_x^1 = D_x^3 = 0$ . In contrast, for the 2NN bond along  $(-1, 1, 0)$ , the bond midpoint lies on both the perpendicular-bisector mirror (which exchanges the sites) and a mirror that contains the bond (which does not). The first again enforces  $\mathbf{D} \perp$  bond; the sec-

ond requires  $\mathbf{D}$  to be odd under reflection, i.e. parallel to the in-plane normal of that mirror (perpendicular to the bond and within the plane), which eliminates the out-of-plane component:  $D_z^2 = 0$ .

Remarkably, the DMI is comparable in magnitude to the components of the anisotropic exchange: The ratio between the Frobenius norm of  $J^1$  ( $|J^1| = 2.92$ ) and Euclidean norm of  $\mathbf{D}^1$  ( $|\mathbf{D}^1| = 0.90$ ) is  $|\mathbf{D}^1|/|J^1| = 0.31$ . This implies the strength of the DMI is relatively large, as the typical value of this ratio is on the order of 0.1 [48, 62]. We see that the role of the DMI may be significant, implying consequences such as the stabilization of non-collinear spin structures.

#### IV. STRAIN TUNING

Given the potential for frustration in  $\text{Nb}_3\text{Cl}_8$ , we explore its magnetism further using biaxial strain tuning to better understand and manipulate its magnetic characteristics. We expect the  $S=1/2$  trimerization to persist under biaxial strain since the symmetry is not broken. We used the four-state energy mapping technique to calculate magnetic anisotropy parameters as we applied compressive and tensile strain. We applied biaxial strain in our DFT calculations by changing the  $a$  and  $b$  lattice vectors by the same percentage, and relaxing atom positions before running self-consistent field calculations for four-state mapping. For computational efficiency in generating exchange vs. strain diagrams, we use a slightly lower energy cutoff for the plane-wave basis set (350 eV) compared to the cases that we explore using Monte Carlo calculations (400 eV) in Section III. We see from Supplementary Material D that the exchange parameters extracted in both cases are similar to each other.

We find that the diagonal components of  $J^1$  and  $J^3$  in Eq. (3) can change sign with compressive strain, indicating switching between AFM and FM interactions, as illustrated in Fig. 3. Other magnetic interaction parameters, including components of the DMI vector, can change sign and magnitude due to strain as well. We discuss those results in the Supplementary Material E.

Due to the change of magnetic exchange, the biaxial strain tunes the short-range magnetic correlations from antiferromagnetic, paramagnetic to ferromagnetic, evident from the magnetic susceptibility data within three test cases: 0%,  $-3\%$  and  $-4\%$ . For 0% strain, we have the results in Eq. (3), and for  $-3\%$ , we got single-ion anisotropy  $A = 0.46$  meV and, using the same conven-

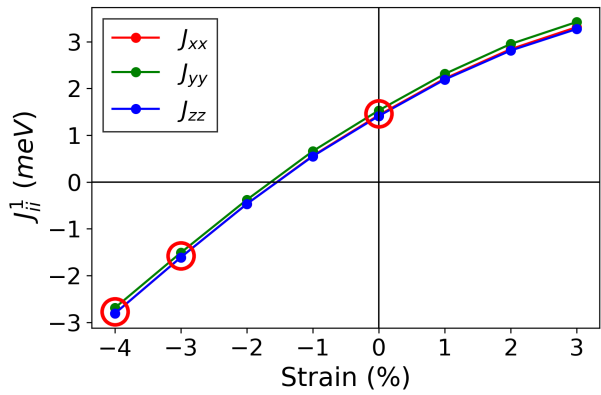
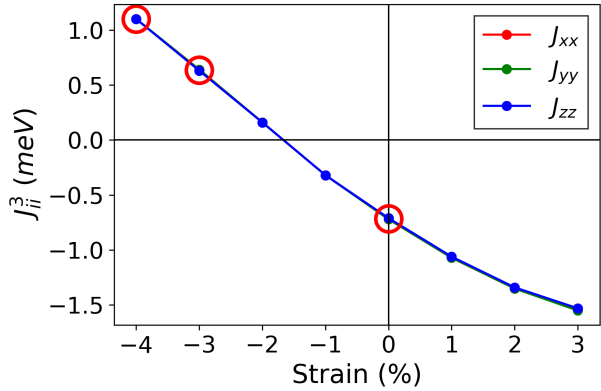
(a) Diagonal matrix elements of  $J^1$  (meV) vs strain (%)(b) Diagonal matrix elements of  $J^3$  (meV) vs strain (%)

FIG. 3: Diagonal matrix elements  $J_{xx}$ ,  $J_{yy}$  and  $J_{zz}$  of  $J^1$  and  $J^3$ , with respect to strain (horizontal axis). Note that some of the  $J_{xx}$ ,  $J_{yy}$ ,  $J_{zz}$  curves in each case heavily overlap with each other. The red circles highlight the three test cases explored in our Monte Carlo calculations: 0%, -3% and -4%.

tion in Eq. (4), the anisotropic exchange:

$$J^1 = \begin{bmatrix} -1.57 & -0.34 & 0.61 \\ 0.33 & -1.47 & 0.00 \\ -0.62 & 0.00 & -1.57 \end{bmatrix}, J^2 = \begin{bmatrix} 0.71 & 0.00 & 0.06 \\ 0.00 & 0.72 & -0.03 \\ -0.07 & 0.04 & 0.71 \end{bmatrix}$$

$$J^3 = \begin{bmatrix} 0.63 & 0.00 & 0.00 \\ 0.00 & 0.63 & 0.00 \\ 0.00 & 0.00 & 0.63 \end{bmatrix} \quad (6)$$

For -4% strain, we got single-ion anisotropy  $A = 0.43$  meV and anisotropic exchange:

$$J^1 = \begin{bmatrix} -2.79 & -0.38 & 0.48 \\ 0.39 & -2.69 & 0.01 \\ -0.47 & 0.01 & -2.79 \end{bmatrix}, J^2 = \begin{bmatrix} 0.63 & 0.00 & 0.06 \\ 0.00 & 0.62 & -0.04 \\ -0.06 & 0.03 & 0.62 \end{bmatrix}$$

$$J^3 = \begin{bmatrix} 1.10 & 0.00 & 0.00 \\ 0.00 & 1.10 & 0.00 \\ 0.00 & 0.00 & 1.10 \end{bmatrix} \quad (7)$$

Using these parameters in Monte Carlo simulations, for -3% strain, we got  $(\theta_x, \theta_y, \theta_z) = (-0.6 \pm 0.4, 0.8 \pm 0.4, -1.2 \pm 0.4)$ ; and for -4% we got  $(12.6 \pm 0.4, 12.4 \pm 0.4, 11.6 \pm 0.4)$ . See Fig. 2 and Fig. S4 for the Monte Carlo susceptibility and fitting data. Since  $\theta_d$  for -3% strain are very close to 0, it is reasonable to infer that we are close to paramagnetism. For -4% strain, we clearly have at least short-range FM correlations since  $\theta_d > 0$ . The phonon dispersions in Supplementary Material G show that the structures are stable.

The above results on strain-dependent exchange interactions and short-range correlations do not themselves establish the presence or absence of long-range magnetic order in the ground state. To further assess the magnetic tendencies, we directly compared the total energies of representative magnetic configurations.

We perform *ab initio* supercell and spin-spiral calculations as consistency checks to show that the unstrained and -4% strained structures have energies close to the energies of standard commensurate 120° AFM and FM states, respectively. For the unstrained structure, this is consistent with recent works which suggest that monolayer Nb<sub>3</sub>Cl<sub>8</sub> has a 120° AFM ground state [18, 26, 33], where the 120° order is defined on the triangular lattice of Nb<sub>3</sub> trimers (each treated as an effective  $S = 1/2$  moment), i.e., the relative spin angles are between *intratrimer* Nb<sub>3</sub> units rather than between *intratrimer* Nb atoms. However, due to the significant DMI we observe, it is reasonable to expect the true ground states to be incommensurate.

For the *ab initio* supercell calculations, we choose possible magnetic configurations that are commensurate with the supercell cell: FM, stripe (using a  $2 \times 2$  supercell), and 120° order ( $\sqrt{3} \times \sqrt{3}$  supercell). With SOC included, we tested several different spatial and orientational alignment of spins in each configuration (e.g., 120° with spins pointing inwards vs. outwards for a reference triangle; stripes along horizontal and vertical directions; and in-plane vs out-of-plane FM configurations). We found that for 0% strain, the 120° configurations yielded the lowest energy per unit cell, with stripe configurations being higher by about 0.39 meV per unit cell, and the FM configurations being higher than 120° order by about 1.55 meV. In comparison, for -4% strain, the FM configurations have the lowest energy, with the 120° configurations being higher by about 2.05 meV per unit cell, and stripe configurations being higher than FM by about 2.45 meV. Thus, while genuinely incommensurate states are inaccessible in single-supercell calculations, the energetics of the accessible commensurate configurations point to ground-state order close to 120° AFM at 0% strain and FM at -4% strain.

Next, we perform additional calculations based on spin-spirals without SOC, following the approach of Ref. [26] (see Supplementary Material H for more information). As seen in Fig. 4, for 0% strain, the minimum of the spin-spiral dispersion occurs at the  $K$  point, which is consistent with 120° AFM order. For -4% strain, the

minimum lies close to the  $\Gamma$  point (0.08 meV away from the energy at  $\Gamma$ , with the total energy variation between the maximum and minimum being 2.52 meV). This implies a tendency towards FM order. These trends agree qualitatively with the strain-tunable magnetic behavior demonstrated by the four-state mapping and supercell calculations with SOC.

All these observations suggest that  $\text{Nb}_3\text{Cl}_8$  exhibits a strain-tunable magnetic response, making it a promising material to explore short-range AFM, PM, and FM correlations for future applications.

## V. CONCLUSION

Our findings provide deeper insights into the magnetic behavior of  $\text{Nb}_3\text{Cl}_8$ . We showed that monolayer  $\text{Nb}_3\text{Cl}_8$  may be magnetically frustrated. This result supports recent work that suggests exotic magnetic phenomena in  $\text{Nb}_3\text{Cl}_8$ . Even though our classical Monte Carlo calculations do not capture quantum fluctuations, the AFM interaction and frustration index  $f > 1$  indicate the possibility of  $\text{Nb}_3\text{Cl}_8$  being a quantum spin liquid, due to the spin-1/2 nature of the system and the strong quantum fluctuations. These ground states are very exciting due to the wide array of potential applications in exploring fundamental quantum mechanics, quantum computing, spintronics, and the development of advanced materials with novel magnetic and electronic properties. We further showed that the short-range correlations may be tuned between AFM, PM and FM using strain, which is appealing due to the demand for controllable magnetic properties in quantum materials technologies. A poten-

tial next step would be to identify the role of the observed relatively-significant DMI, and confirm whether it can stabilize exotic non-collinear spin structures such as spin spirals or skyrmions. Further explorations could also involve establishing a comprehensive phase diagram for the system. By elucidating the role of magnetic anisotropy and extended interactions, our work paves the way for further theoretical and experimental studies aimed at harnessing the unique properties of  $\text{Nb}_3\text{Cl}_8$  for applications in condensed matter research, device engineering, and beyond.

## VI. ACKNOWLEDGMENTS

This material is primarily based upon work supported by the National Science Foundation under Award No. DMR-2339995. Part of the work used advanced algorithm and codes supported by the Computational Materials Sciences Program funded by the U.S. Department of Energy, Office of Science, Basic Energy Sciences, Materials Sciences, and Engineering Division, PNNL FWP 83557. This research used resources of the National Energy Research Scientific Computing Center, a DOE Office of Science User Facility supported by the Office of Science of the U.S. Department of Energy under Contract No. DE-AC02-05CH11231 using NERSC award BES-ERCAP0033256. This work was facilitated through the use of advanced computational, storage, and networking infrastructure provided by the Hyak supercomputer system and funded by the University of Washington Molecular Engineering Materials Center at the University of Washington (NSF MRSEC DMR-2308979).

---

[1] K. S. Burch, D. Mandrus, and J.-G. Park, Magnetism in two-dimensional van der waals materials, *Nature* **563**, 47 (2018).

[2] X. Jiang, Q. Liu, J. Xing, N. Liu, Y. Guo, Z. Liu, and J. Zhao, Recent progress on 2d magnets: Fundamental mechanism, structural design and modification, *Applied Physics Reviews* **8** (2021).

[3] S. Zhang, R. Xu, N. Luo, and X. Zou, Two-dimensional magnetic materials: structures, properties and external controls, *Nanoscale* **13**, 1398 (2021).

[4] D. Li, S. Li, C. Zhong, and J. He, Tuning magnetism at the two-dimensional limit: A theoretical perspective, *Nanoscale* **13**, 19812 (2021).

[5] S. Yu, J. Tang, Y. Wang, F. Xu, X. Li, and X. Wang, Recent advances in two-dimensional ferromagnetism: strain-, doping-, structural-and electric field-engineering toward spintronic applications, *Science and technology of advanced materials* **23**, 140 (2022).

[6] I. Žutić, J. Fabian, and S. D. Sarma, Spintronics: Fundamentals and applications, *Reviews of modern physics* **76**, 323 (2004).

[7] B. Zhang, P. Lu, R. Tabrizian, P. X.-L. Feng, and Y. Wu, 2d magnetic heterostructures: Spintronics and quantum future, *npj Spintronics* **2**, 6 (2024).

[8] C. L. Degen, F. Reinhard, and P. Cappellaro, Quantum sensing, *Reviews of modern physics* **89**, 035002 (2017).

[9] P. Mendels and A. Wills, Introduction to frustrated magnetism, *Springer Series in Solid-State Sciences* **164** (2011).

[10] L. Balents, Spin liquids in frustrated magnets, *nature* **464**, 199 (2010).

[11] C. Broholm, R. J. Cava, S. Kivelson, D. Nocera, M. Norman, and T. Senthil, Quantum spin liquids, *Science* **367**, eaay0668 (2020).

[12] J. P. Sheckelton, *Strongly correlated molecular magnetism in triangular-lattice cluster materials*, Ph.D. thesis, Johns Hopkins University (2015).

[13] Y. Haraguchi, C. Michioka, M. Ishikawa, Y. Nakano, H. Yamochi, H. Ueda, and K. Yoshimura, Magnetic-nonmagnetic phase transition with interlayer charge disproportionation of nb3 trimers in the cluster compound nb3cl8, *Inorganic Chemistry* **56**, 3483 (2017).

[14] C. M. Pasco, I. El Baggari, E. Bianco, L. F. Kourkoutis, and T. M. McQueen, Tunable magnetic transition to a singlet ground state in a 2d van der waals layered trimerized kagomé magnet, *ACS nano* **13**, 9457 (2019).

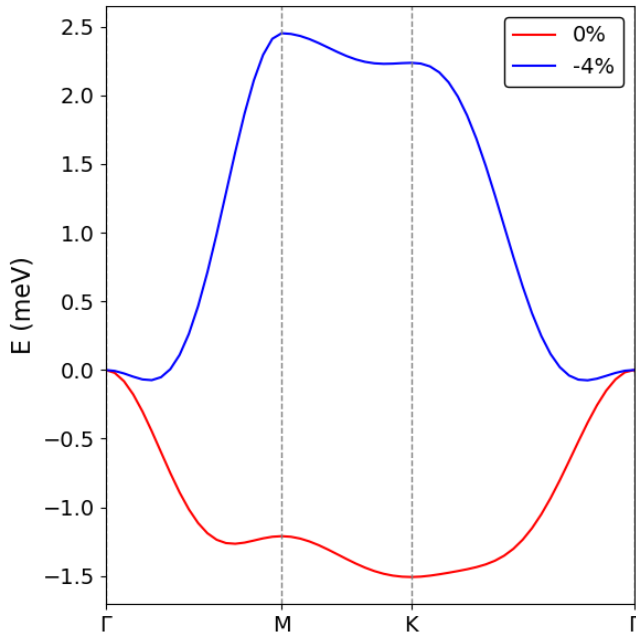


FIG. 4: Spin-spiral energies as a function of ordering vector for 0% and  $-4\%$  biaxial strain, with the energy at  $\Gamma$  set to 0.

- [15] J. P. Scheckelton, K. W. Plumb, B. A. Trump, C. L. Broholm, and T. M. McQueen, Rearrangement of van der waals stacking and formation of a singlet state at  $t=90$  k in a cluster magnet, *Inorganic Chemistry Frontiers* **4**, 481 (2017).
- [16] J. Hu, X. Zhang, C. Hu, J. Sun, X. Wang, H.-Q. Lin, and G. Li, Correlated flat bands and quantum spin liquid state in a cluster mott insulator, *Communications Physics* **6**, 172 (2023).
- [17] B. Liu, Y. Zhang, X. Han, J. Sun, H. Zhou, C. Li, J. Cheng, S. Yan, H. Lei, Y. Shi, *et al.*, Possible quantum-spin-liquid state in van der waals cluster magnet nb<sub>3</sub>cl<sub>8</sub>, *Journal of Physics: Condensed Matter* **36**, 155602 (2024).
- [18] S. Grytsiuk, M. I. Katsnelson, E. G. v. Loon, and M. Rösner, Nb<sub>3</sub>cl<sub>8</sub>: a prototypical layered mott-hubbard insulator, *npj Quantum Materials* **9**, 8 (2024).
- [19] S. Gao, S. Zhang, C. Wang, S. Yan, X. Han, X. Ji, W. Tao, J. Liu, T. Wang, S. Yuan, *et al.*, Discovery of a single-band mott insulator in a van der waals flat-band compound, *Physical Review X* **13**, 041049 (2023).
- [20] Y. Zhang, Y. Gu, H. Weng, K. Jiang, and J. Hu, Mottness in two-dimensional van der waals nb<sub>3</sub> x 8 monolayers (x= cl, br, and i), *Physical Review B* **107**, 035126 (2023).
- [21] E. A. Stepanov, Signatures of a charge ice state in the doped mott insulator nb<sub>3</sub> cl<sub>8</sub>, *arXiv preprint arXiv:2405.19114* (2024).
- [22] J. Yoon, E. Lesne, K. Sklarek, J. Scheckelton, C. Pasco, S. S. Parkin, T. M. McQueen, and M. N. Ali, Anomalous thickness-dependent electrical conductivity in van der waals layered transition metal halide, nb<sub>3</sub>cl<sub>8</sub>, *Journal of Physics: Condensed Matter* **32**, 304004 (2020).
- [23] Y. Haraguchi and K. Yoshimura, Molecular orbital electronic instability in the van der waals kagome semiconductor nb<sub>3</sub> cl<sub>8</sub>: Exploring future directions, *arXiv preprint arXiv:2407.19457* (2024).
- [24] R. Nakamura, D. Takegami, K. Fujinuma, M. Nakamura, M. Ferreira-Carvalho, A. Melendez-Sans, M. Yoshimura, K.-D. Tsuei, Y. Haraguchi, H. Aruga Katori, *et al.*, Charge fluctuations in a cluster mott state: Hard x-ray photoemission study on a breathing kagome magnet nb<sub>3</sub> cl<sub>8</sub>, *Physical Review B* **110**, L081109 (2024).
- [25] K. Momma and F. Izumi, Vesta: a three-dimensional visualization system for electronic and structural analysis, *Applied Crystallography* **41**, 653 (2008).
- [26] J. Mangeri, V. R. Pavizhakumari, and T. Olsen, Magnetoelectric behavior of breathing kagomé monolayers of nb<sub>3</sub>(cl,br,i)<sub>8</sub> from first-principles calculations, *arXiv preprint arXiv:2411.04839* (2024).
- [27] H. Liu, S. Meng, and F. Liu, Screening two-dimensional materials with topological flat bands, *Physical Review Materials* **5**, 084203 (2021).
- [28] N. Regnault, Y. Xu, M.-R. Li, D.-S. Ma, M. Jovanovic, A. Yazdani, S. S. Parkin, C. Felser, L. M. Schoop, N. P. Ong, *et al.*, Catalogue of flat-band stoichiometric materials, *Nature* **603**, 824 (2022).
- [29] D. Călugăru, A. Chew, L. Elcoro, Y. Xu, N. Regnault, Z.-D. Song, and B. A. Bernevig, General construction and topological classification of crystalline flat bands, *Nature Physics* **18**, 185 (2022).
- [30] J. Duan, D.-S. Ma, R.-W. Zhang, Z. Zhang, C. Cui, W. Jiang, Z.-M. Yu, and Y. Yao, Inventory of high-quality flat-band van der waals materials, *arXiv preprint arXiv:2204.00810* (2022).
- [31] D. A. Jeff, F. Gonzalez, K. Harrison, Y. Zhao, T. Fernando, S. Regmi, Z. Liu, H. R. Gutierrez, M. Neupane, J. Yang, *et al.*, Raman study of layered breathing kagome lattice semiconductor nb<sub>3</sub>cl<sub>8</sub>, *2D Materials* **10**, 045030 (2023).
- [32] Z. Sun, H. Zhou, C. Wang, S. Kumar, D. Geng, S. Yue, X. Han, Y. Haraguchi, K. Shimada, P. Cheng, *et al.*, Ob-

ervation of topological flat bands in the kagome semiconductor nb3cl8, *Nano Letters* **22**, 4596 (2022).

[33] J. Aretz, S. Grytsiuk, X. Liu, G. Feraco, C. Knekna, M. Waseem, Z. Dan, M. Bianchi, P. Hofmann, M. N. Ali, *et al.*, From strong to weak correlations in breathing-mode kagome van der waals materials: Nb  $\_3$ (f, cl, br, i)  $\_8$  as a robust and versatile platform for many-body engineering, arXiv preprint arXiv:2501.10320 (2025).

[34] Q. Yang, M. Wu, J. Duan, Z. Ma, L. Li, Z. Huo, Z. Zhang, K. Watanabe, T. Taniguchi, X. Zhao, *et al.*, Gate tunable room-temperature mott insulator in kagome compound nb3cl8, arXiv preprint arXiv:2506.08730 (2025).

[35] Y. Lu, K. Zhao, T. Zhang, and B. Dong, Bipolar nb3cl8 field effect transistors, *Magnetochemistry* **10**, 43 (2024).

[36] B. Lee, X. Zhang, J. Kang, B. J. Jeong, S. Cho, K. H. Choi, J. Jeon, S. H. Lee, D. Kim, Y. H. Kim, *et al.*, A negative photoconductivity photodetector based on two-dimensional nb 3 cl 8, *Nanoscale* **16**, 20312 (2024).

[37] B. Bradlyn, L. Elcoro, J. Cano, M. G. Vergniory, Z. Wang, C. Felser, M. I. Aroyo, and B. A. Bernevig, Topological quantum chemistry, *Nature* **547**, 298 (2017).

[38] Y. Lu, H. Wang, X. Xu, L. Wang, and L. Yang, Intrinsic magnetoelectric coupling induced by the flat bands in kagome van der waals multiferroic heterostructures, *Physical Review B* **111**, 165410 (2025).

[39] X. Yang, Y. Zeng, M. Pan, M. Jiang, C. Hu, and Q. Feng, Electronic and optical properties of cri3/nb3cl8 heterojunction: a first principles investigation, *Journal of Physics: Condensed Matter* **37**, 235501 (2025).

[40] M. Khan, N. U. Din, D. R. Englund, and M. N. Leuenberger, Multiferroic dark excitonic mott insulator in the breathing-kagome lattice material nb  $\_3$  cl  $\_8$ , arXiv preprint arXiv:2412.13456 (2024).

[41] J. Kim, Y. Lee, Y. W. Choi, T. S. Jung, S. Son, J. Kim, H. J. Choi, J.-G. Park, and J. H. Kim, Terahertz spectroscopy and dft analysis of phonon dynamics of the layered van der waals semiconductor nb3 x 8 (x= cl, i), *ACS omega* **8**, 14190 (2023).

[42] A. Bouhmouche, A. Jabar, I. Rhrissi, and R. Moubah, Highly optical anisotropy, electronic and thermodynamic properties of the topological flat bands kagome nb3cl8, *Materials Science in Semiconductor Processing* **175**, 108238 (2024).

[43] J. Jiang, Q. Liang, R. Meng, Q. Yang, C. Tan, X. Sun, and X. Chen, Exploration of new ferromagnetic, semiconducting and biocompatible nb 3 x 8 (x= cl, br or i) monolayers with considerable visible and infrared light absorption, *Nanoscale* **9**, 2992 (2017).

[44] J. Cenker, S. Sivakumar, K. Xie, A. Miller, P. Thijssen, Z. Liu, A. Dismukes, J. Fonseca, E. Anderson, X. Zhu, *et al.*, Reversible strain-induced magnetic phase transition in a van der waals magnet, *Nature Nanotechnology* **17**, 256 (2022).

[45] B. Mortazavi, X. Zhuang, and T. Rabczuk, A first-principles study on the physical properties of two-dimensional nb3cl8, nb3br8 and nb3i8, *Applied Physics A* **128**, 934 (2022).

[46] Band structure and magnetism diagrams are provided in Supplementary Material I.

[47] H. Xiang, E. Kan, S.-H. Wei, M.-H. Whangbo, and X. Gong, Predicting the spin-lattice order of frustrated systems from first principles, *Physical Review B—Condensed Matter and Materials Physics* **84**, 224429 (2011).

[48] H. Xiang, C. Lee, H.-J. Koo, X. Gong, and M.-H. Whangbo, Magnetic properties and energy-mapping analysis, *Dalton Transactions* **42**, 823 (2013).

[49] D. Šabani, C. Bacaksiz, and M. Milošević, Ab initio methodology for magnetic exchange parameters: Generic four-state energy mapping onto a heisenberg spin hamiltonian, *Physical Review B* **102**, 014457 (2020).

[50] H. Zhang, Z. Shi, Z. Jiang, M. Yang, J. Zhang, Z. Meng, T. Hu, F. Liu, L. Cheng, Y. Xie, *et al.*, Topological flat bands in 2d breathing-kagome lattice nb3tecl7, *Advanced Materials* **35**, 2301790 (2023).

[51] Otherwise, we would have the general form  $A_{i,xx}(S_i^x)^2 + A_{i,yy}(S_i^y)^2 + A_{i,zz}(S_i^z)^2 + 2A_{i,xy}S_i^x S_i^y + 2A_{i,xz}S_i^x S_i^z + 2A_{i,yz}S_i^y S_i^z$  [48]. In our case, we have  $A_i(S^z)^2 \equiv (A_{i,zz} - A_{i,xx})(S_i^z)^2$ .

[52] S. Saadatmand, B. Powell, and I. McCulloch, Phase diagram of the spin-1 2 triangular  $j_1 - j_2$  heisenberg model on a three-leg cylinder, *Physical Review B* **91**, 245119 (2015).

[53] C. Glittum and O. F. Syljuåsen, Arc-shaped structure factor in the  $j_1 - j_2 - j_3$  classical heisenberg model on the triangular lattice, *Physical Review B* **104**, 184427 (2021).

[54] R. Bishop and P. Li, Spin-gap study of the spin- $\frac{1}{2}$   $j_1 - j_2$  model on the triangular lattice, arXiv preprint arXiv:1508.00414 (2015).

[55] S.-S. Gong, W. Zhu, J.-X. Zhu, D. N. Sheng, and K. Yang, Global phase diagram and quantum spin liquids in a spin-1 2 triangular antiferromagnet, *Physical Review B* **96**, 075116 (2017).

[56] Y.-F. Jiang and H.-C. Jiang, Nature of quantum spin liquids of the  $s=1/2$  heisenberg antiferromagnet on the triangular lattice: A parallel dmrg study, *Physical Review B* **107**, L140411 (2023).

[57] N. Van Hinh and P. T. T. Nga, Magnetic properties of the spin-1  $j_1 - j_2 - j_3$  heisenberg model on a triangular lattice, in *Journal of Physics: Conference Series*, Vol. 2744 (IOP Publishing, 2024) p. 012003.

[58] The magnetic parameters between different trimer pairs will differ by rotations of the exchange matrices Eq. (4); for instance, by  $60^\circ$  for adjacent NN trimer pairs.

[59] S. Mugiraneza and A. M. Hallas, Tutorial: a beginner's guide to interpreting magnetic susceptibility data with the curie-weiss law, *Communications Physics* **5**, 95 (2022).

[60] Y. Zhou, X. Han, J. Luo, D. Wu, A. Fang, B. Shen, B. Feng, Y. Shi, J. Yang, and R. Zhou, Antiferromagnetic spin fluctuations and structural transition in cluster mott insulator candidate nb3cl8 revealed by 93nb-and 35cl-nmr, *Chinese Physics Letters* (2025).

[61] A. Ramirez *et al.*, Strongly geometrically frustrated magnets, *Annual Review of Materials Science* **24**, 453 (1994).

[62] T. Moriya, Anisotropic superexchange interaction and weak ferromagnetism, *Physical review* **120**, 91 (1960).

[63] G. Kresse and J. Furthmüller, Efficiency of ab-initio total energy calculations for metals and semiconductors using a plane-wave basis set, *Computational materials science* **6**, 15 (1996).

[64] G. Kresse and J. Furthmüller, Software vasp, vienna (1999), *Phys. Rev. B* **54**, 169 (1996).

[65] G. Kresse and J. Hafner, Ab initio molecular dynamics for liquid metals, *Physical review B* **47**, 558 (1993).

[66] G. Kresse, Hafner, j1: Cas: 528: Dyak2cxkvfkrt14% 3d: Ab initio molecular-dynamics simulation of the

liquid-metal-amorphous-semiconductor transition in germanium. vol. 49, *Phys Rev B* , 14251 (1994).

[67] G. Kresse and J. Hafner, Ab initio molecular-dynamics simulation of the liquid-metal–amorphous-semiconductor transition in germanium, *Physical Review B* **49**, 14251 (1994).

[68] P. E. Blöchl, Projector augmented-wave method, *Physical review B* **50**, 17953 (1994).

[69] G. Kresse and D. Joubert, From ultrasoft pseudopotentials to the projector augmented-wave method, *Physical review b* **59**, 1758 (1999).

[70] W. Kohn and L. J. Sham, Self-consistent equations including exchange and correlation effects, *Physical review* **140**, A1133 (1965).

[71] We caution the reader that since we used a  $4 \times 4 \times 1$  supercell, we are not excluding interactions between periodic images when calculating magnetic anisotropy parameters between third-nearest-neighbors (i.e.,  $J_{ij}^3$ ). So, we deviate from the standard four-state energy mapping technique in the 3NN case by accounting for this change in coordination number by dividing all computed  $J_{ij}^3$  by 2 since each interaction occurs twice for this choice of supercell. A  $5 \times 5 \times 1$  (or larger) supercell would have mitigated this issue. However, we could only converge our calculations for the collinear Heisenberg case with a  $5 \times 5 \times 1$  supercell despite experimenting with a wide range of *LAMBDA* and Wigner-Seitz radii for the noncollinear case. Despite this, we confirm that the isotropic Heisenberg  $J^4$  from 4NN interactions is negligible using the collinear case. This justifies truncating interactions past 3NN interactions even using the four-state mapping method. This is consistent with other works like Ref. [26] considering interactions only until 3NN, and our own spin-spiral calculations mapping to the spin-1/2 Heisenberg model for the case without SOC (which gave  $J^4 = 0$  meV, as seen in Supplementary Material H).

[72] S. Magonov, P. Zönnchen, H. Rotter, H. Cantow, G. Thiele, J. Ren, and M. Whangbo, Scanning tunneling and atomic force microscopy study of layered transition metal halides nb3x8 (x= cl, br, i), *Journal of the American Chemical Society* **115**, 2495 (1993).

[73] S. L. Dudarev, G. A. Botton, S. Y. Savrasov, C. Humphreys, and A. P. Sutton, Electron-energy-loss spectra and the structural stability of nickel oxide: An lsda+ u study, *Physical Review B* **57**, 1505 (1998).

[74] J.-X. Xiong, X. Zhang, and A. Zunger, Role of magnetic and structural symmetry breaking in forming the mott insulating gap in nb 3 cl 8, *Physical Review B* **111**, 155122 (2025).

[75] R. F. Evans, W. J. Fan, P. Chureemart, T. A. Ostler, M. O. Ellis, and R. W. Chantrell, Atomistic spin model simulations of magnetic nanomaterials, *Journal of Physics: Condensed Matter* **26**, 103202 (2014).

[76] C. Lin, S. Poncé, and N. Marzari, General invariance and equilibrium conditions for lattice dynamics in 1d, 2d, and 3d materials, *npj Computational Materials* **8**, 236 (2022).

[77] F. Libbi, N. Bonini, and N. Marzari, Thermomechanical properties of honeycomb lattices from internal-coordinates potentials: the case of graphene and hexagonal boron nitride, *2D Materials* **8**, 015026 (2020).

## SUPPLEMENTARY MATERIAL

### Supplementary Material A: Density Functional Theory calculation details

An *ab initio* density functional theory (DFT) approach was implemented to perform first-principles DFT+U+SOC calculations using the *Vienna Ab initio Simulation Package* (VASP) version 6.4.1 [63–67], for Hubbard  $U$  and spin-orbit coupling (SOC). The valence electron and core interactions were described using the projector augmented wave (PAW) method [68, 69]. For the exchange-correlation energy functional, we used the local density approximation (LDA) [70]. Within the applied PAW pseudopotentials, we included semicore 4s and 4p states as valence electrons for Nb, and only the standard 3s and 3p states as valence electrons for Cl. We used a  $4 \times 4 \times 1$  supercell for the monolayer [71]. Since lattice parameter information from experiment is not available for the monolayer, we used the parameters  $a = 6.744 \text{ \AA}$  and  $\alpha = 120^\circ$  from single-crystal X-ray diffraction data for  $\alpha\text{-Nb}_3\text{Cl}_8$  [72], which is the multi-layer high-temperature structure that is proposed to lead to exotic spin phenomena and remain in the  $\alpha$  phase at low temperatures if exfoliated at high temperatures [14, 17, 18]. A vacuum spacing of  $25 \text{ \AA}$  along the  $c$ -direction was applied to avoid interactions between periodic images of the monolayers. We used a  $1 \times 1 \times 1$   $\Gamma$ -centered mesh with automatically-determined  $k$  points. The conjugate-gradient algorithm was used to relax only the atom positions until the norms of all the forces were smaller than  $10^{-7} \text{ eV/\AA}$ . To account for the in-plane anisotropy, all Nb magnetic moments were constrained along the  $x$  direction during structural relaxation. Prior to computing the single-ion anisotropy constants, we confirmed the in-plane anisotropy by comparing total energies for several collinear configurations in which all Nb moments were constrained to point along the same direction  $\hat{\mathbf{m}} = (m_x, m_y, m_z)$ . The resulting energies increase in the following order:  $E_{(1,0,0)} = E_{(0,1,0)} = E_{(-1,1,0)} = E_{(1,1,0)} = E_{(-\sqrt{3},-1,0)} < E_{(1,-\sqrt{3},0)} = E_{(-1/2,\sqrt{3}/2,0)} < E_{(0,1,1)} = E_{(1,0,1)} < E_{(0,0,1)}$ . Taking  $E_{(1,0,0)}$  as the reference, the energy differences  $\Delta E = E - E_{(1,0,0)}$  (in meV) for the above directions are: 0, 0, 0, 0, 0, 0.020, 0.021, 0.050, 0.050, 0.081. Because the relaxed crystal structure is insensitive to the choice among the lowest-energy initial magnetic-moment configurations, we fixed all Nb moments along the  $x$  direction during structural relaxation as a convenient and representative choice.

We set the magnetic moments of  $\text{Nb}_3$  trimers by assigning to each Nb atom the same initial magnetic moment, to correspond to the desired moment of a triangle vertex point. In order to accurately capture the shared spin-1/2 moment, we constrained the direction and sign of the assigned moment for each spin configuration, but not the size (which we let the software determine). The convergence criterion of the total energy was  $10^{-8} \text{ eV}$ .

The energy cutoff for the plane-wave basis set was 400 eV (except for the  $J_{ij}^k$  vs. strain plots Fig. 3 (of the main text), and Fig. 6,7 here, which use 350 eV; see main text for clarification). We used Gaussian smearing, with a smearing width of 0.03 eV. The Wigner-Seitz radii for Nb and Cl were 1.270 Å and 1.111 Å respectively; and the *LAMBDA* parameter (which sets the weight with which the penalty terms of the constrained local moment approach enter into the total energy expression and the Hamiltonian) was set to 9. The simplified (rotationally invariant) approach to DFT+U introduced by Dudarev et al. [73] was used to incorporate the DFT+U formalism. A Hubbard potential of  $U = 1$  eV was used on Niobium d orbitals to account for effective on-site Coulomb interactions. Our optimized structure yielded an Nb-Nb bond length of 2.8112 Å within an Nb<sub>3</sub> trimer. This is only 0.01% different from the experimental bond length of 2.8109 in Ref. [13, 23], although it is quite different from the 2.85 Å bond length in Ref. [74].

#### Supplementary Material B: Monte Carlo calculation details

For our classical Monte Carlo calculations, we used VAMPIRE 6.0 [75] with the parameters computed using DFT. Due to the system's anisotropy, we do not expect  $\chi_d$  to always be the same for different  $d$ .  $\theta_d$  can be easily found by fitting the linear portion of  $\chi_d^{-1}$  vs.  $T$  data to a line, and calculating  $T$  at which  $\chi_d^{-1} = 0$ . This is simply the negative of the vertical intercept  $b$  divided by the gradient  $m$ :  $-b/m$ . The propagated uncertainty  $\sigma_\theta$  of  $\theta_d$  (without the small covariance term) is calculated using  $\sigma_\theta \approx \sqrt{\left(\frac{\sigma_b}{m}\right)^2 + \left(\frac{b\sigma_m}{m^2}\right)^2}$ , where  $\sigma_b$  is the standard error of  $b$ , and  $\sigma_m$  is the standard error of the  $m$ .  $C$  in Eq. (2) (of the main text) is the inverse of the gradient, and then the effective magnetic moment is  $\mu_{\text{eff}} = \sqrt{8C}\mu_B$  (for the Bohr magneton  $\mu_B$ ). For a spin-1/2 moment, we expect  $\mu_{\text{eff}} \approx 1.73\mu_B$  [59]. When fitting our data to a line, we used the data only above 50 K, in order to ensure we are within the paramagnetic region for which the Curie-Weiss law is applicable, well above the kinks in susceptibility that arise at or below  $\sim 20$  K in all our cases (e.g., in Fig. 2 (of the main text)). In our susceptibility plots Fig. 2 (of the main text) and Fig. 8, the equations of the linear fits are given in the inset in the top-left along with the coefficient of determination  $R^2$ . The  $R^2$  values very close to 1 indicate that the fits explain the variance in data quite well.

Unless otherwise stated, we employed a 2D triangular lattice of size 100 × 100 nm, with periodicity in the x and y directions. This yields 25628 atoms for the unstrained structure, 27234 atoms for the -3% biaxial strained structure, and 27900 atoms for the -4% biaxial strained structure. We modeled the triangular lattice in VAMPIRE using a 2D rectangular 'unit cell' of dimensions  $a \times a\sqrt{3} \times 1000$  (for lattice vector  $a$  and

'vacuum spacing' 1000), with two Nb<sub>3</sub> 'atoms' placed at (0.25, 0.75, 0) and (0.75, 0.25, 0) in fractional coordinates. We used temperature increments of 0.2 K,  $2.5 \times 10^6$  equilibration time steps, and  $2.5 \times 10^6$  loop time steps. We additionally assigned the initial spins to be in random directions.

#### Supplementary Material C: Origin of DMI constraints

The DMI vectors extracted from Eq. (3) (of the main text) for the unstrained case are  $\mathbf{D}^1 = (0, -0.89, -0.15)$  meV,  $\mathbf{D}^2 = (-0.02, -0.04, 0)$  meV, and  $\mathbf{D}^3 = (0, 0, 0)$  meV.  $\mathbf{D}^1$  is visualized in Fig. 5.

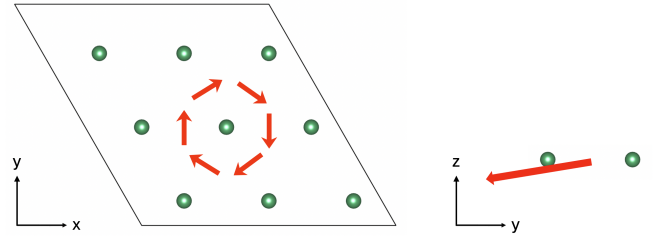


FIG. 5:  $\mathbf{D}^1$  for the unstrained case, visualized in the  $xy$  (left) and  $yz$  (right) planes. The  $D_z$  component is -0.15 meV for all NN bonds.

#### Supplementary Material D: Anisotropic exchange and single-ion anisotropy for unstrained structure with plane-wave basis energy cutoff of 350 eV

Using a plane-wave basis energy cutoff of 350 eV, we get a single-ion anisotropy of 0.56 meV (same as with 400 eV), and the anisotropic exchange in Eq. (D1). These values are very close to the values for 400 eV given in the main text Eq. (3) (of the main text).

$$J^1 = \begin{bmatrix} 1.44 & 0.16 & -0.88 \\ -0.16 & 1.52 & 0.00 \\ 0.88 & 0.00 & 1.40 \end{bmatrix}, J^2 = \begin{bmatrix} 0.96 & 0.00 & 0.04 \\ 0.00 & 0.96 & -0.04 \\ -0.04 & 0.04 & 0.96 \end{bmatrix}$$

$$J^3 = \begin{bmatrix} -0.72 & 0.00 & 0.00 \\ 0.00 & -0.72 & 0.00 \\ 0.00 & 0.00 & -0.72 \end{bmatrix} \quad (D1)$$

#### Supplementary Material E: Strain tuning data

We present results on the behavior of magnetic anisotropy parameters that are excluded from the main text for NN interactions and single-ion anisotropy in Fig. 6, and for 2NN interactions in Fig. 7. Note that for all percentages of strain applied, the non-diagonal com-

ponents of  $J^3$  (and therefore DMI) are 0 up to our 2 decimal place accuracy.

#### Supplementary Material F: Additional susceptibility data

We present susceptibility data for the  $y$  and  $z$  directions in Fig. 8.

#### Supplementary Material G: Phonon dispersions showing structural stability

We use phonon dispersions to show that our structures are stable for the 0,  $-3\%$  and  $-4\%$  biaxial strained cases. We used VASP to perform Density Functional Perturbation Theory (DFPT) calculations for the monolayer unit cell with SOC, with unconstrained Nb magnetic moments starting in the  $(1, 0, 0)$  direction. Otherwise, the calculation details are as in Supplementary Material A.

Indeed, we see from Fig. 9 that the phonon frequencies are positive and imply stable structures. Note that there is a small pocket of negative frequencies near  $\Gamma$ , with the minima of the negative frequencies being  $\sim -0.27$  THz for 0%,  $\sim -0.22$  THz for  $-3\%$  and  $\sim -0.21$  THz for  $-4\%$ . These small values lie within the  $\sim -1$  THz threshold commonly attributed to numerical noise near the  $\Gamma$  point [76, 77], and is therefore not indicative of a true structural instability.

#### Supplementary Material H: Spin-spiral calculations

We performed spin-spiral calculations without SOC, because VASP's spin-spiral implementation uses the generalized Bloch theorem: Adding SOC couples spin and lattice degrees of freedom, and thereby breaks the spin-

rotation invariance required for the spiral boundary conditions. Due to the lack of SOC, the results in this section are intended only as a qualitative reference and not as a replacement for the SOC-based results in the main text.

We computed the spin-spiral dispersion for the unstrained and  $-4\%$  biaxial strained structures. The spiral energies were fitted to an isotropic spin-1/2  $J_1-J_2-J_3-J_4$  Heisenberg model of the following form (using notation consistent with Eq. (1) (of the main text)):

$$H = \sum_{i < j} J_{ij}^k \mathbf{S}_i \cdot \mathbf{S}_j,$$

from which excellent linear fits were obtained (see Fig. 4 (of the main text)). For 0% strain the best fit parameters were

$$(J^1, J^2, J^3, J^4) = (0.99, 0.22, 0.35, 0.00) \text{ meV},$$

and for  $-4\%$  strain the parameters were

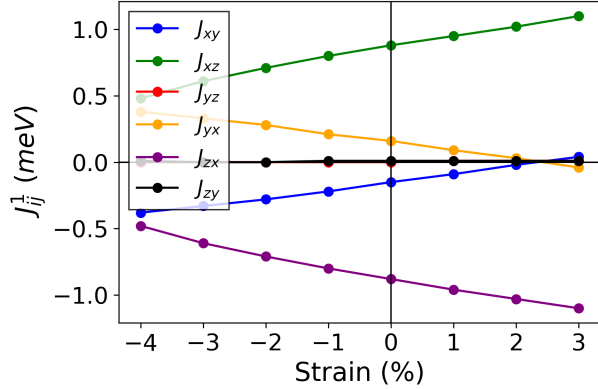
$$(J^1, J^2, J^3, J^4) = (-2.72, 0.27, 0.73, 0.00) \text{ meV}.$$

The extracted exchange constants differ from those obtained from the four-state mapping method because SOC is not included in the spin-spiral calculations and therefore the anisotropic contributions to the exchange constants are absent. However, in both cases, we still see dominant AFM  $J^1$  for 0% strain, and dominant FM  $J^1$  for  $-4\%$  strain.

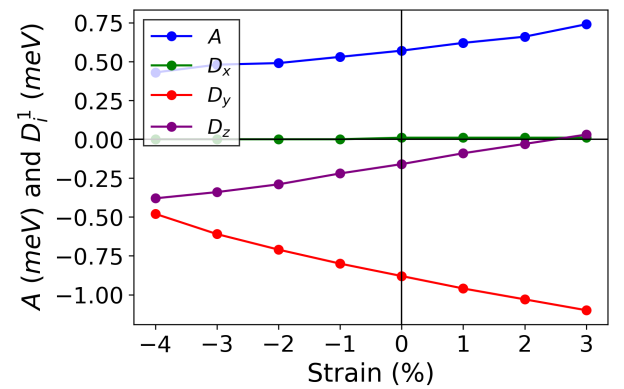
#### Supplementary Material I: Band diagrams and magnetism

For completeness, we present band diagrams for monolayer  $\text{Nb}_3\text{Cl}_8$  in Fig. 10 (a)-(c). We note that our band diagram for the case without spin polarization Fig. 10 (a) compares well with diagrams from other references, such as Ref. [18, 32] even though they used PBE as the exchange-correlation energy functional (compared to the LDA we used).

We also present a plot of magnetization in Fig. 10 (d).

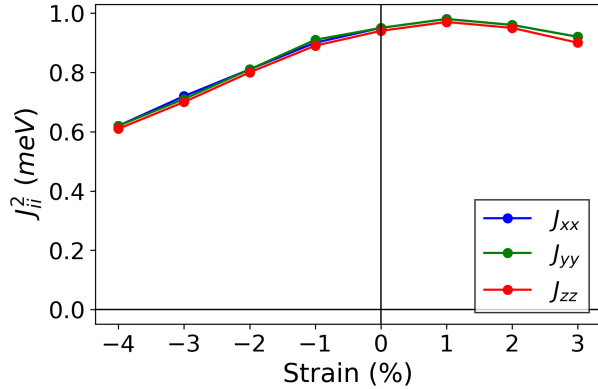


(a) Non-diagonal matrix elements of  $J^1$  (meV) vs strain (%)

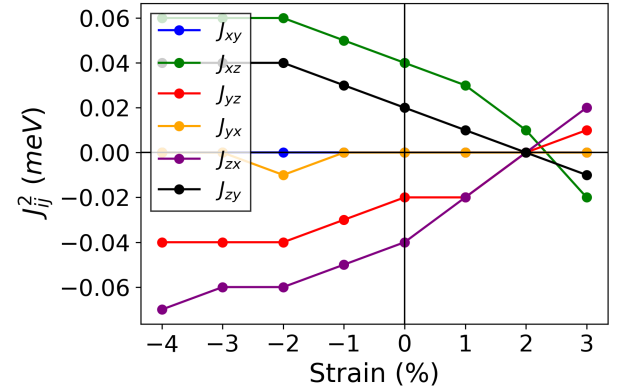


(b) Components of DMI vector  $\mathbf{D}^1 = (D_x, D_y, D_z)$  (meV) and single-ion anisotropy  $A$  (meV) vs strain (%)

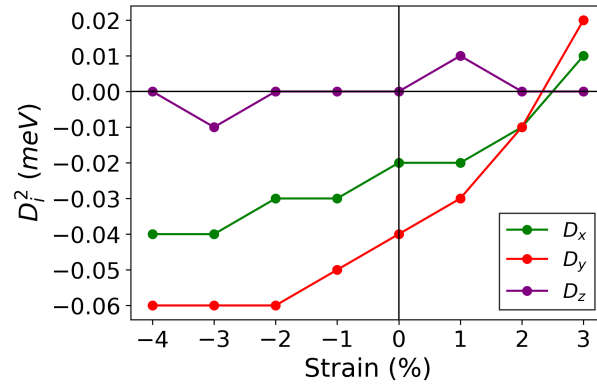
FIG. 6: Non-diagonal elements of  $J^1$ , DMI from NN interactions, and single-ion anisotropy, with respect to strain.



(a) Diagonal matrix elements of  $J^2$  (meV) vs strain (%)



(b) Non-diagonal matrix elements of  $J^2$  (meV) vs strain (%)



(c) Components of DMI vector  $\mathbf{D}^2 = (D_x, D_y, D_z)$  (meV) vs strain (%)

FIG. 7: Diagonal elements of  $J^2$ , non-diagonal elements of  $J^2$ , and DMI from 2NN interactions, with respect to strain.

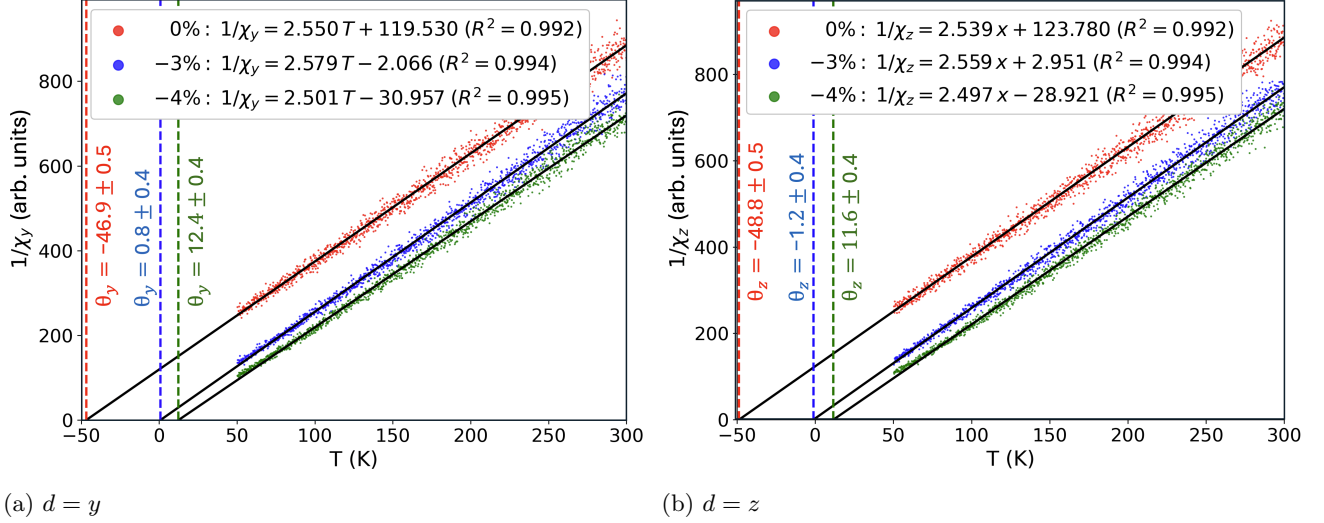


FIG. 8: Inverse susceptibility  $1/\chi_d$  (arb. units) vs. temperature  $T(K)$  in the  $d = y$  and  $d = z$ -directions for 0%, -3%, and -4% biaxial strain. Notation is as used in Fig. 2 (of the main text).

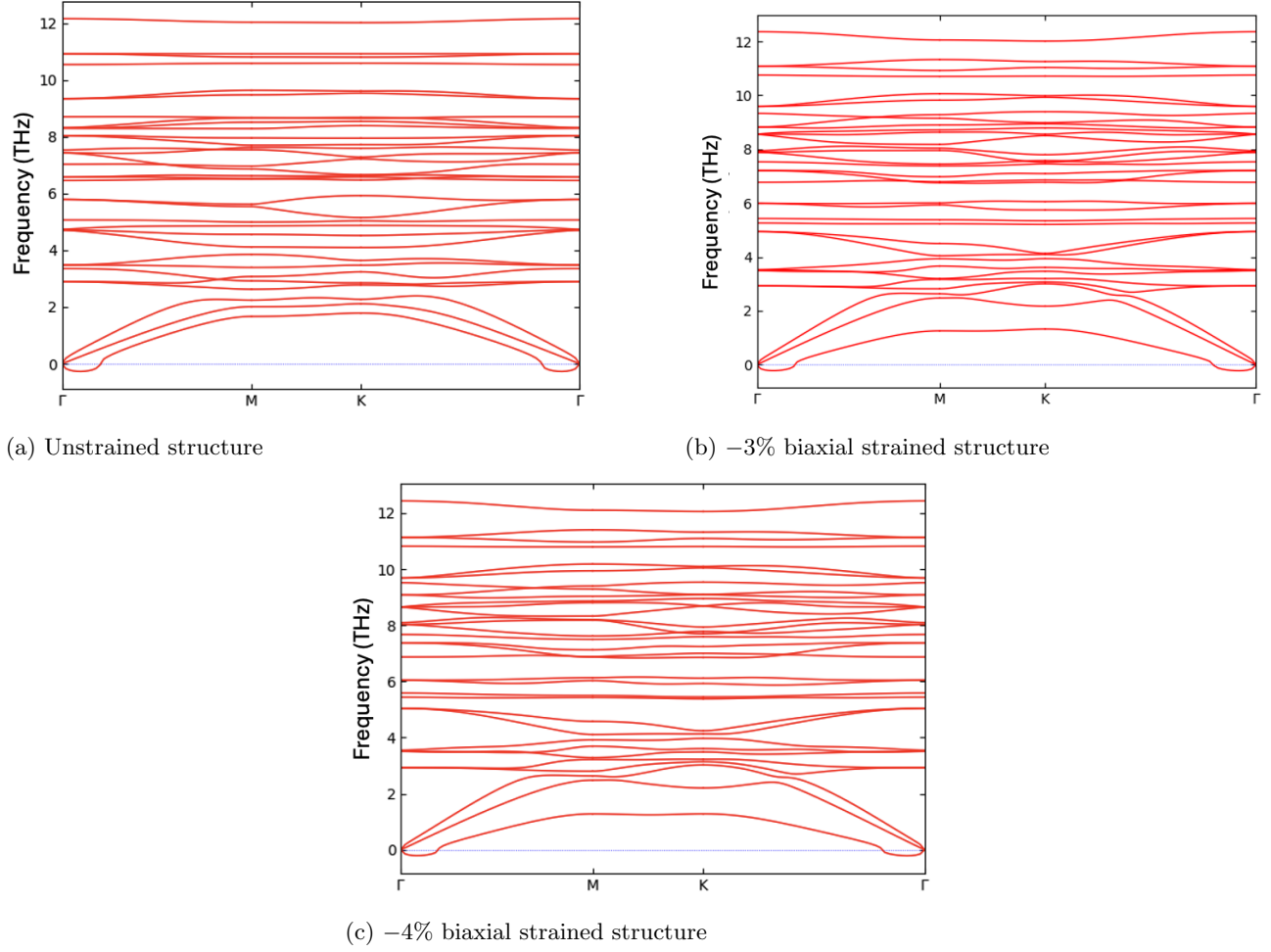
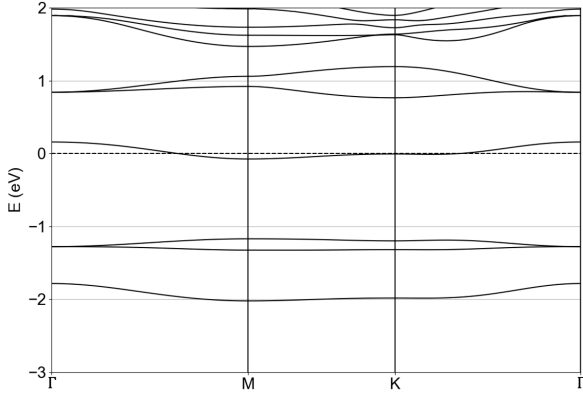
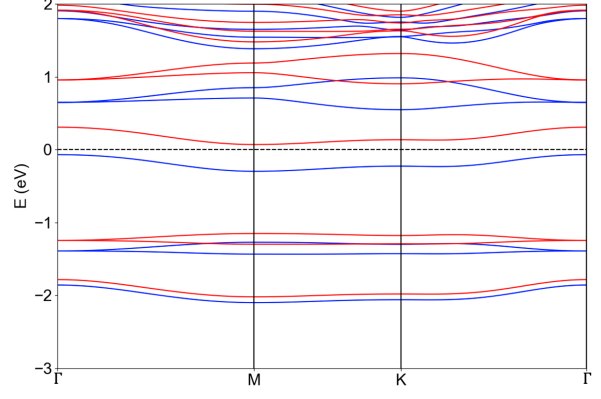


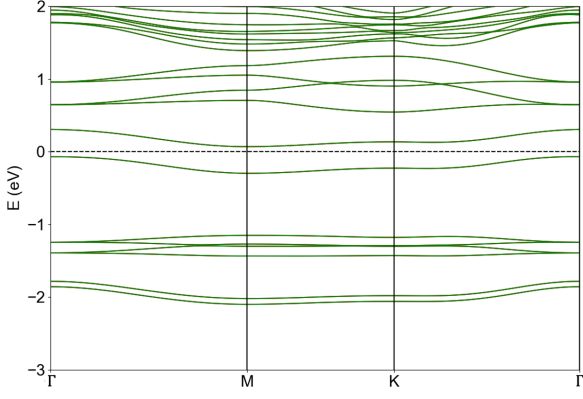
FIG. 9: Phonon dispersions.



(a) No spin polarization.



(b) Spin polarized, but without SOC. Blue bands are the spin up channel, and red bands spin down.



(c) With SOC. Bands are doubly-degenerate.

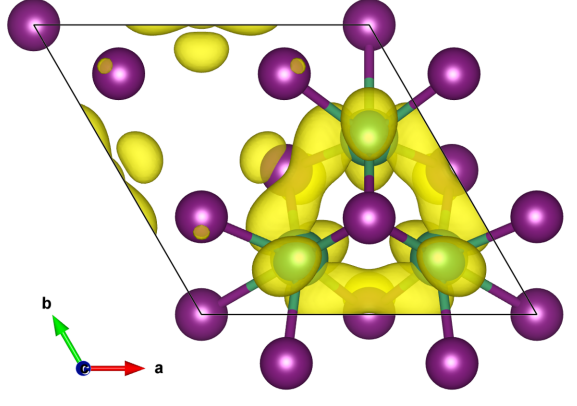
(d) Magnetization in monolayer  $\text{Nb}_3\text{Cl}_8$ .

FIG. 10: (a)-(c) Band diagrams for monolayer  $\text{Nb}_3\text{Cl}_8$  along the path  $\Gamma - M - K - \Gamma$  in the Brillouin zone. (d) Magnetization (yellow) in monolayer  $\text{Nb}_3\text{Cl}_8$  unit cell, viewed from above the  $ab$ -plane. The magnetization is calculated by subtracting the spin up density by the spin down density. Nb atoms are in green, and Cl atoms in purple. Most of the magnetization is from the Nb atoms, while the small yellow bubbles in the top-left are minor contributions from Cl atoms.